Delft University of Technology

Predictive models for energy dissipation in mechanochemical ball milling

Nuñez, Santiago Garrido; Schott, Dingena L.; Padding, Johan T.

Important note
To cite this publication, please use the final published version (if applicable).
Please check the document version above.

Predictive models for energy dissipation in mechanochemical ball milling ☆

Santiago Garrido Nuñez [a],*, Dingena L. Schott [b], Johan T. Padding [a]

[a] Department of Process and Energy, Delft University of Technology, Leeghwaterstraat 39, Delft, 2628 CB, The Netherlands
[b] Department of Maritime and Transport Technology, Delft University of Technology, Mekelweg 2, Delft, 2628 CD, The Netherlands

HIGHLIGHTS

- Master curves allow predictive dissipation capabilities for untested operational conditions.
- Fill ratio influences the contribution of tangential and normal dissipation in the system.
- Mechanical characterization of $NaBH_4$ regeneration is validated by predicting mechanochemical yield.

GRAPHICAL ABSTRACT
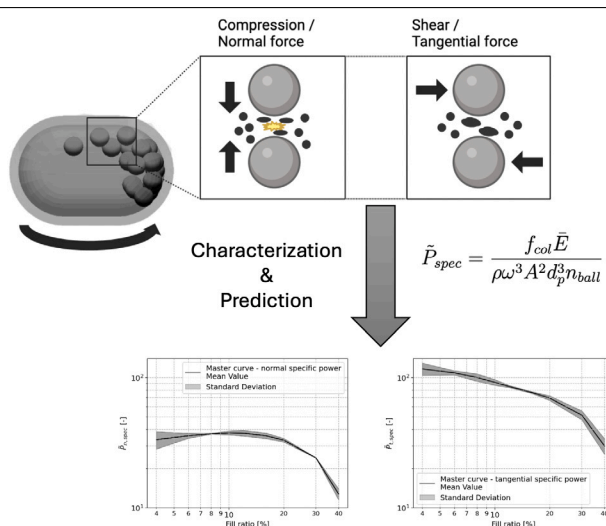
ABSTRACT

High-energy ball milling is a versatile method utilized in mechanochemical reactions and material transformations. Understanding and characterizing the relevant mechanical variables is crucial for the optimization and up-scaling of these processes. To achieve this, the present study delves into differentiating the contributions of normal and tangential interactions during high-energy collisions. Using Discrete Element Method (DEM) simulations, we characterize how operational parameters influence these energy dissipation modes, emphasizing the significance of tangential interactions. Our analysis also reveals how different operational parameters such as ball size, fill ratio, and rotational speed affect the mechanical action inside the milling jar giving rise to multiple operating zones where different modes of energy dissipation can thrive. Finally, we present master curves that generalize findings across a wide range of configurations, offering a tool for characterizing and predicting mechanochemical processes beyond the presented cases. These results provide a robust framework for improving mechanochemical reaction efficiency, and equipment design.

1. Introduction

High-energy ball milling is a versatile method that harnesses mechanical forces to drive physical and chemical material transformations. In recent years, it has emerged as an attractive technique that can support green chemistry, offering synthesis capabilities without reliance on organic solvents or extreme temperature–pressure conditions [1,2]. Its application in various domains, such as sodium borohydride ($NaBH_4$) mechanochemical regeneration, showcases the growing preference for this novel mechanical method over traditional chemical routes [3]. It has also opened up the possibility of obtaining stable supramolecular and organic compounds that would otherwise be hard or impossible to obtain with traditional methods [2]. Additionally, it has been shown to facilitate ultra-fine grinding and the amorphization of crystalline materials below glass transition temperatures [4,5]. Nonetheless, regardless of the application, an important challenge lies in comprehending and predicting the key mechanical dissipation interactions that influence the success of the process and that are fundamental for optimization and up-scaling [6].

Laboratory-scale milling processes are typically carried out in machines known as ball mills. The function and usage of these machines can vary according to the motion they induce, the size and density of the milling balls used to impact the processed material, and the shape of the container where they are placed. For example, shaker ball mills follow a linear left-to-right motion promoting head-on impacts between the milling balls where normal energy transfer dominates and are typically used with small samples. On the other hand, planetary ball mills use centrifugal forces by inducing a double-axis rotational motion. These centrifugal forces contribute towards tangential energy transfer and attempt to emulate the working mechanism behind industrial-sized roller mills in which potential energy is exploited, offering a direct path for scaling up [2]. However, these are only two general types of ball mills. As applications diversify and increase in complexity, specialized milling machines tailored to distinct motions and mechanical phenomena emerge. While the use of specialized machinery may offer benefits to individual use cases, it also highlights a pressing challenge: the lack of fundamental understanding regarding the underlying phenomenology makes reproducibility across different devices and scales problematic [1,2].

Currently, some control on the outcome of a milling process can be offered with the definition of operational parameters, such as rotational speed or fill ratio. However, it has become apparent that when the process's complexity increases or efficiency and scale-up become relevant, this is no longer sufficient [1]. We hypothesize that distinguishing between normal and tangential energetic contributions in ball milling becomes critical due to their distinct mechanical effects. Normal interactions predominantly induce compression forces, causing direct contact and facilitating material compaction or deformation. In contrast, tangential interactions induce shear forces, resulting in sliding or relative motion between surfaces. Understanding these distinctions is vital as they dictate energy transfer mechanisms, influencing the extent of particle deformation and the resultant effects, such as fragmentation, amorphization, or chemical conversion.

To tackle these limitations, some attempts have been made to characterize milling processes from the point of view of the fundamental mechanics inside the milling jar. Chen et al. [7] make use of DEM (Discrete Element Method) simulations to study the dynamics of a shaker ball mill and quantitatively describe the collision events that take place during a mechanical alloying process. The research focused on the energy dissipation that occurs as a result of ball–ball and ball–wall interactions by analyzing the changes in kinetic energy before and after collision. Although the study provides valuable information, it falls short in distinguishing between the roles of normal and tangential dissipation caused by impact and shearing collisions, which affect how the processed material is treated. Following a similar approach, Broseghini et al. [8] studied how varying the shape of the milling jar

affected the efficiency of a high-energy planetary mill. To do this, an upper bound of the energy available for grinding is approximated using the same principles of kinetic energy transformation, with the main difference that the velocity vectors are decomposed into their normal and tangential components to distinguish the contribution of impacts and shearing. While this approach allows a more in-depth analysis of the different mechanical phenomena inside the jar, the approximations assume that the milling balls do not rotate and the contact model used is not capable of taking into account the non-linear elastic contact behavior of ball–ball and ball–wall interactions. Moreover, we hypothesize that assessing the interaction between the ball and the wall by measuring the change in kinetic energy will not accurately reflect the true extent of the impact. This is because the energy transferred from the wall to the ball could increase the ball's kinetic energy, making it challenging to precisely determine the amount of energy dissipated.

In the field of mechanochemistry, Burmeister et al. [9,10] employed DEM simulations to examine the impact of various stressing conditions in planetary ball mills to obtain Knoevenagel synthesis. To achieve a more accurate representation of the ball–ball and ball–wall interactions, the Hertz–Mindlin model was used. However, their analysis is centered around the dissipation of energy in the normal direction due to head-on collisions, which may be insufficient in cases where shearing has the potential of being a critical component to determine the success of the process [11]. Moreover, the characterization parameters presented are limited to the reactants used and cannot be generalized any further.

Lastly, in the field of ultra-fine milling and particle breakage, Oliveira et al. [12] and Rodriguez et al. [5] have employed a state-of-the-art mechanistic and phenomenological model (UFRJ) to characterize the breakage mechanisms that occur in vertical stir mills and planetary ball mills, respectively. The model has only been validated for normal collisions and as such, the tangential component is typically ignored. This is a limitation that can underestimate the resulting product of the process, as noted by Beinert et al. [13]. In an attempt to overcome this, Oliveira et al. account for the tangential contribution by matching the model predictions with experimental data via back-fitting. This method enables good agreement between experimental and simulation results given that the proportion of tangential contribution is accurately adjusted but, naturally, is susceptible to over-fitting and possible misinterpretation of results. Moreover, this method is viable given that the process involves only a physical transformation (i.e. particle size reduction). In a process where a chemical transformation is expected, such as mechanochemistry, the back-fitting recursion method becomes inadequate. This limitation arises because the Discrete Element Method (DEM) is unable to simulate chemical processes, thus neglecting the possible role of tangential energy dissipation that could influence the rate of a chemical reaction. In other words, it becomes impossible to match experimental and simulation results because the simulations cannot predict the chemical component of the process.

2. Model and methods

2.1. Modeling approach

The Discrete Element Method (DEM) is used to simulate the interactions between the jar and the grinding media. In this study, Altair EDEM 2021.2 was used as the DEM solver and Python 3.9.12 was used for data post-processing. EDEM follows a soft sphere approach by calculating the contact forces for each particle interaction using Hertz and Mindlin's contact model. Then, Newton's laws of motion are used to calculate the instantaneous motion for each particle:

$$m_i \frac{d\mathbf{V}_i}{dt} = \mathbf{F}_{c,i} + m_i \mathbf{g} \tag{1}$$

$$I_i \frac{d\boldsymbol{\omega}_i}{dt} = \boldsymbol{\tau}_i \tag{2}$$

where m_i, I_i, $\mathbf{V}_i$ and $\boldsymbol{\omega}_i$ are the mass, moment of inertia, velocity, and angular velocity, respectively, of particle i. $\mathbf{F}_{c,i}$ and $\boldsymbol{\tau}_i$ represent the total contact force and total contact torque (relative to the particle's center of mass), respectively. The total force and torque are determined by summing over all neighbors in contact with particle i.

The Hertz–Mindlin model [14,15] is selected to calculate the contact force on each pair because it is capable of capturing the non-linear behavior of particle–particle and particle–geometry interactions. The original model was modified to make the damping components accessible for data post-processing. Each discrete element has its own radius R, mass m, Young's modulus Y, shear modulus G, coefficient of restitution e, and Poisson ratio v. The contact force $\mathbf{F}_{c,ij}$ on a particle i due to its interaction with another particle j (or wall) is the vector sum of a normal $\mathbf{F}_{n,ij}$ and tangential $\mathbf{F}_{t,ij}$ force:

$$\mathbf{F}_{c,ij} = \mathbf{F}_{n,ij} + \mathbf{F}_{t,ij} = (K_n \delta_{n,ij} - \gamma_n \mathbf{V}_{n,ij}) + (K_t \delta_{t,ij} - \gamma_t \mathbf{V}_{t,ij}) \quad (3)$$

with:

$$K_n = \frac{4}{3} Y^* \sqrt{R^* \delta_n} \quad (4)$$

$$\gamma_n = -2\sqrt{\frac{5}{6}} \beta \sqrt{S_n m^*} \geq 0 \quad (5)$$

$$K_t = 8 G^* \sqrt{R^* \delta_n} \quad (6)$$

$$\gamma_t = -2\sqrt{\frac{5}{6}} \beta \sqrt{S_t m^*} \geq 0 \quad (7)$$

$$S_n = 2 Y^* \sqrt{R^* \delta_n} \quad (8)$$

$$S_t = 8 G^* \sqrt{R^* \delta_n} \quad (9)$$

$$\beta = \frac{\ln(e)}{\sqrt{\ln^2(e) + \pi^2}} \quad (10)$$

$$\frac{1}{Y^*} = \frac{(1 - v_1^2)}{Y_1} + \frac{(1 - v_2^2)}{Y_2} \quad (11)$$

$$\frac{1}{G^*} = \frac{2(2 - v_1)(1 + v_1)}{Y_1} + \frac{2(2 - v_2)(1 + v_2)}{Y_2} \quad (12)$$

$$\frac{1}{R^*} = \frac{1}{R_1} + \frac{1}{R_2} \quad (13)$$

$$\frac{1}{m^*} = \frac{1}{m_1} + \frac{1}{m_2} \quad (14)$$

Here, $\mathbf{V}_{n,ij}$ and $\mathbf{V}_{t,ij}$ are the relative normal and tangential velocities between the two particles i and j at the point of contact. $\delta_{n,ij}$ and $\delta_{t,ij}$ represent the normal and tangential overlap vectors between the particles, the latter being found by integrating the relative tangential velocity with time and projecting it on the current tangential direction. K_n and K_t are the elastic coefficients for normal and tangential contact. Furthermore, γ_n and γ_t represent the viscoelastic damping coefficients for the normal and tangential contacts. On the right-hand side of Eq. (3), the first term between parenthesis is the normal force, and the second term is the tangential force. The normal force has two terms, a spring force and a normal damping force $\mathbf{F}_{n,d}$. The tangential force also has two terms, a shear force and a tangential damping force $\mathbf{F}_{t,d}$.

Additionally, the contact torque $\boldsymbol{\tau}_{ij}$ on particle i due to its interaction with particle (or wall element) j is calculated by cross multiplying the vector $\mathbf{R}_{ij}$, which points from the center of mass of particle i to the contact point with particle j, by the tangential contact force $F_{t,ij}$. Since the particles undergo constant rolling motion, especially against the wall, it is also necessary to account for slight non-sphericity with a rolling torque $\boldsymbol{\tau}_{r,ij}$ calculated by the coefficient of rolling friction μ_r, magnitude of the normal contact force $F_{n,ij}$, the distance from the center of mass to the contact point R_{ij} and the orientation of the angular velocity vector $\boldsymbol{\omega}_{rel}$ of the particle relative to the particle (or wall) it is in contact with:

$$\boldsymbol{\tau}_{ij} = \mathbf{R}_{ij} \times \mathbf{F}_{t,ij} + \boldsymbol{\tau}_{r,ij} \quad (15)$$

$$\boldsymbol{\tau}_{r,ij} = -\mu_r F_{n,ij} R_{ij} \frac{\boldsymbol{\omega}_{rel}}{\omega_{rel}} \quad (16)$$

Table 1
Mesh settings.

Parameter	Value
Minimum mesh scaling factor	0.33
Maximum mesh scaling factor	4
Maximum deviation scaling factor	1
Maximum angle	0.261 [rad]

Lastly, the amount of dissipated energy in a time interval t_1 to t_2, attributed to the damping components γ_n and γ_t, can be calculated as follows:

$$E_n = \int_{t_1}^{t_2} \mathbf{F}_{n,d} \cdot \mathbf{V}_{n,ij} \, dt = \int_{t_1}^{t_2} \gamma_n V_{n,ij}^2 \, dt \quad (17)$$

$$E_t = \int_{t_1}^{t_2} \mathbf{F}_{t,d} \cdot \mathbf{V}_{t,ij} \, dt = \int_{t_1}^{t_2} \gamma_t V_{t,ij}^2 \, dt \quad (18)$$

2.2. Simulation setup and calibration

In this work, we model a commercially available ball mill. In particular, the Emax high-energy ball mill is a device produced and distributed by the German company Retsch. It offers a novel approach to ball milling by combining high friction and impact results with a temperature control system allowing for controlled grinding. The machine can allocate proprietary grinding jars with 125 ml of volume that follow a circular motion with a rotational speed n up to 2000 revolutions per minute (corresponding to an angular frequency of $\omega = 2\pi n/60 = 209$ rad/s with an amplitude (radius) A of 1.7 cm, see Fig. 1. The movement of the jar has been replicated in our simulations. To accurately represent the geometry of the milling jar, a CAD file was imported into EDEM and an automatic rigid body mesh was built using the settings in Table 1.

The system is initialized by generating the total amount of discrete media over a span of five seconds, allowing them to reach resting positions inside the jar before any movement is induced. The simulation is then run for an additional 15 s to observe the system's dynamics. To minimize the computational complexity of the model, the number of discrete elements has been limited to only include the milling balls. This approach is viable as the influence of the processed material can be represented by altering the friction and restitution coefficients [16–18].

As a result, two sets of coefficients are used. The first set corresponds to a clean, empty jar without powder, serving as a reference for the unaltered dynamics of the milling balls. The second set was obtained through calibration, considering the presence of hydrated sodium metaborate ($NaBO_2 \cdot 4H_2O$) and magnesium hydride (MgH_2). The calibration methodology combines the approaches of Dreizin et al. [17] and Burmeister et al. [10]. For an accurate calibration, it is essential to have a representative powder layer covering the jar and milling balls. To achieve this, we selected one of the experimental conditions from our previous work, where we explored the effects of various experimental parameters on the mechanochemical regeneration of $NaBH_4$ [19]. The selected conditions involve a ball-to-powder ratio of 30, a 66% molar ratio excess, a milling time of 12.5 h, a fill ratio of 10%, and a rotational speed of 600 rpm, ultimately enabling a regeneration yield of 71%. After conducting this experiment, the resulting powder layer inside the jar provides the most accurate representation of how the powder's presence affects the balls and jar, enabling a precise calibration process.

The methodology for determining the restitution coefficient is based on free-fall experiments. Milling balls were removed from the jar, and for each test, a ball was randomly selected and dropped onto the flat bottom surface of the milling jar. The restitution coefficient was then calculated as the ratio between the drop height and the bounce height, as shown in Eq. (19). A total of 32 tests were conducted to ensure
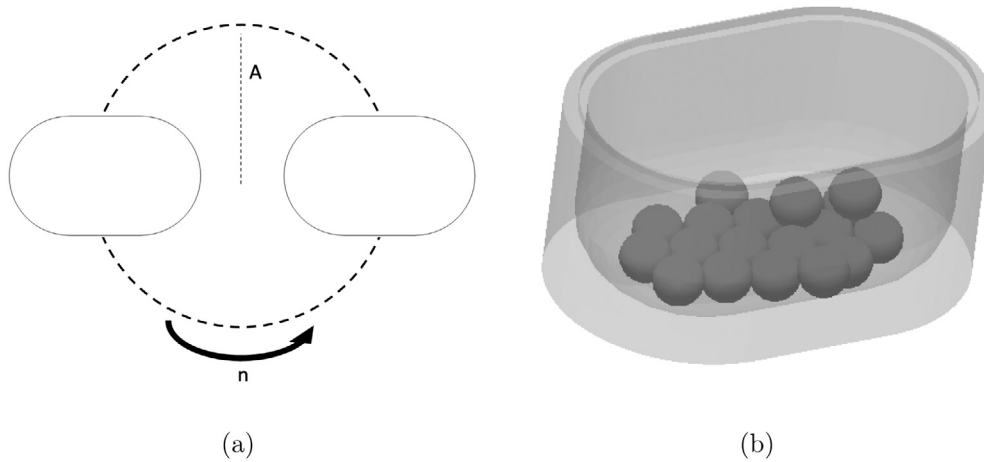
(a) (b)

Fig. 1. (a) Schematic of jar movement (b) 3D model of the jar.
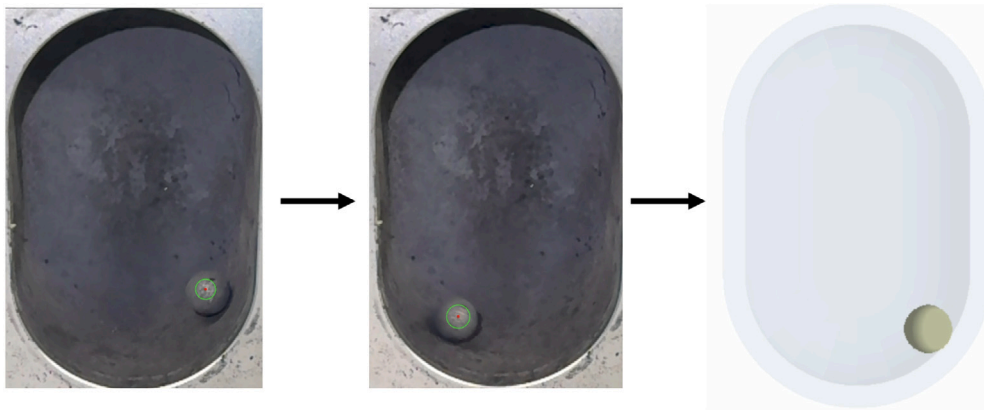

Fig. 2. Frame of video and simulation used for the calibration of the friction coefficients.

statistical significance, and the average value of 0.3 was chosen as the calibrated restitution coefficient.

$$e = \sqrt{\frac{h_{bounce}}{h_{drop}}} \qquad (19)$$

The calibration of the friction coefficients involves the combination of a new experiment and its computational representation using the previously defined restitution coefficient as a constant. In this experiment, the representative powder layer is retained, but instead of the flat surface at the bottom of the jar, the walls are used. The jar is positioned vertically, and a milling ball is placed at the midpoint of the jar's straight wall. The ball is then released, and a custom tracking code records its position as it oscillates along the walls until it comes to rest. An equivalent DEM model of this experiment is created, and the friction coefficients are adjusted until the simulated ball position aligns with the experimental curve. See Figs. 2 and 3 for the calibration results.

The comparison between the experimental and computational curves indicates that a static friction coefficient of 0.3 and a rolling friction coefficient of 0.045 provide a good fit. To further illustrate the sensitivity of the ball's motion to changes in these coefficients, we have included additional values in Fig. 3. Notably, the rolling friction significantly affects the number of oscillations the ball undergoes before reaching its resting state, while the static friction primarily influences the height of each oscillation and the time it takes for the ball to reach its inflection points. Ultimately, both coefficients must be fine-tuned together. This finding aligns with the work of Dreizin et al. [17], but contrasts with Burmeister et al. [10], who suggest that the static friction coefficient has no significant impact. The final calibrated values and

Table 2
Properties used for the milling balls and walls, corresponding to clean steel X46Cr13 (standard values) and calibrated values accounting for the presence of $NaBO_2 \cdot 4H_2O$ and MgH_2. *Note that to speed up the simulations, Young's modulus has been lowered, as discussed in subSection 2.4.

Parameter	Standard value	Calibrated value
Restitution coefficient	0.68 [20]	0.3
Static friction coefficient	0.7 [21]	0.3
Rolling friction coefficient	0.01 [20]	0.045
Density	7700 [kg/m^3] [22]	
Young's modulus	2.05 [MPa]–205* [GPa] [22]	
Poisson's ratio	0.235 [22]	

Table 3
Simulation solver settings.

Parameter	Value
Simulation time step	$9.5 * 10^{-7}$ [s]
Total simulation time	20 [s]
Time integration method	Euler

simulation settings used in the simulations can be found in Tables 2 and 3.

2.3. Analysis of power and granular temperature

Relevant dependent variables are derived from the normal and tangential damping forces shown in Eq. (3). The normal interactions account for head-on collisions while the tangential interactions account
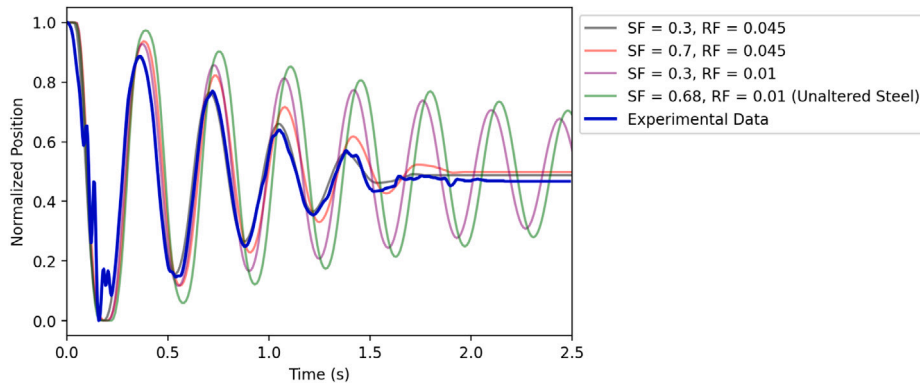
Fig. 3. Normalized ball position as a function of time for calibration purposes. SF: static friction; RF: rolling friction. The bumps during the initial experimental oscillation of the ball are due to inaccuracies of ball detection during initial frames.

for glancing collisions. The benefit of extracting these forces directly from the Hertz–Mindlin model is that it becomes possible to access instantaneous values for both normal and tangential interactions at any time and not rely on averages derived from power calculations. This allows for a more precise representation of the evolution of the energy dissipation given by Eqs. (17) and (18). Thus, it is possible to calculate the mean normal and tangential energy dissipation per collision by summing of all individual dissipation events and dividing by the number of collisions in a given time.

$$\overline{E_n} = \frac{\sum E_n}{N_{collisions}} \tag{20}$$

$$\overline{E_t} = \frac{\sum E_t}{N_{collisions}} \tag{21}$$

Then, the normal and tangential dissipation power can be calculated by multiplying with the collision frequency f_{col} observed within the system:

$$P_n = f_{col}\overline{E_n} \tag{22}$$

$$P_t = f_{col}\overline{E_t} \tag{23}$$

By adding Eqs. (22) and (23) together, the total dissipated power available to the processed material can be calculated. This value could then be compared to the total power of the machine to find an initial estimate of the efficiency of the process. Unfortunately, the Emax is not equipped with a torque sensor so it needs to be estimated from the simulation. In EDEM, each geometry is modeled as a series of triangles, similar to a mesh. Therefore, the total torque on the geometry **T** around the center of rotation $\mathbf{r}_c$ can be calculated as follows:

$$\mathbf{T} = \sum_a \left(\mathbf{r}_a - \mathbf{r}_c\right) \times \mathbf{F}_a + \mathbf{T}_a \tag{24}$$

where $\mathbf{F}_a$ is the total force on triangle a, $\mathbf{r}_a$ the triangle's center of mass, and $\mathbf{T}_a$ the torque on triangle a. With this, it becomes possible to calculate the total power P_{total} to drive the system:

$$P_{total} = \omega\overline{T_z} \tag{25}$$

where $\omega = 2\pi n/60$ is the angular frequency with which the system is driven (n is the shaker frequency in rotations per minute), realizing the rotations of the jar only take place around the z-axis.

The granular temperature (Θ) is an important parameter for the kinetic and hydrodynamic characterization of dynamic granular systems [23]. It is a quantity that measures the variance in the distribution of particle velocities, analogous to the fluctuations in molecular velocity distributions which are measured by the thermodynamic temperature [24]:

$$\Theta = \frac{1}{3}\left(\langle\mathbf{V}^2\rangle - \langle\mathbf{V}\rangle^2\right) \tag{26}$$

where **V** represents the velocity vector of a particle, and pointy brackets $\langle\cdots\rangle$ indicate an average over all particles in a mesh cell dividing the

geometry of the milling jar. In this paper, the granular temperature is used to identify high-energy collision zones within the milling jar. By doing this, it becomes possible to identify different collision regimes as the filling of the jar and the shaking speed change.

2.4. Evaluation of the effect of lowering Young's modulus

Using realistic values for the Young's modulus of steel necessitates using extremely small integration time steps, potentially making the simulations computationally very expensive. A way to tackle this limitation is to artificially lower Young's modulus as shown by Lommen et al. [25]. This is because reducing the stiffness weakens contact forces between particles and allows them to deform more, leading to larger overlaps under the same applied force. This enables particles to change their velocities more gently upon impact.

Lowering the Young's modulus should be done carefully to find a best-performance value where the accuracy of the simulation is preserved while allowing for shorter simulation times. Since the Young's modulus has a direct influence on the damping and elastic components of both tangential and normal forces, as shown in Eq. (3), it influences the energy dissipation per collision. Thus, a sensitivity analysis with 19 discrete media with diameter $d_b = 10$ mm, shown in Fig. 4, was carried out. The total power exerted onto the system, based on Eq. (25) has been measured for different values of Young's modulus, as this allows an analysis of the influence on both the elastic and damping components. By doing this, relevant particle properties, such as velocity and momentum are also included in the decision making. By decreasing the Young's modulus by a factor of 100 (from 205 GPa to 2.05 GPa), we can achieve a threefold reduction in computation time, while remaining within a range of two standard deviations from the mean power predicted for the realistic value. Thus, for all the following simulations, we set Young's modulus to 2.05 GPa.

2.5. Simulation variable parameters

The relevant operational parameters for this study are the rotational speed n, size of the milling balls d_b, and the fill ratio f_r which is defined as the volumetric ratio between the total of all milling balls and that of the empty milling jar. Note that the fill ratio differs from the ratio of the stagnant layer thickness to the jar height because of the void space in a packed bed of mono-dispersed particles. The fill ratios used in the simulations are presented in Table 4. The rotational speed is varied from 600 to 1200 rpm.
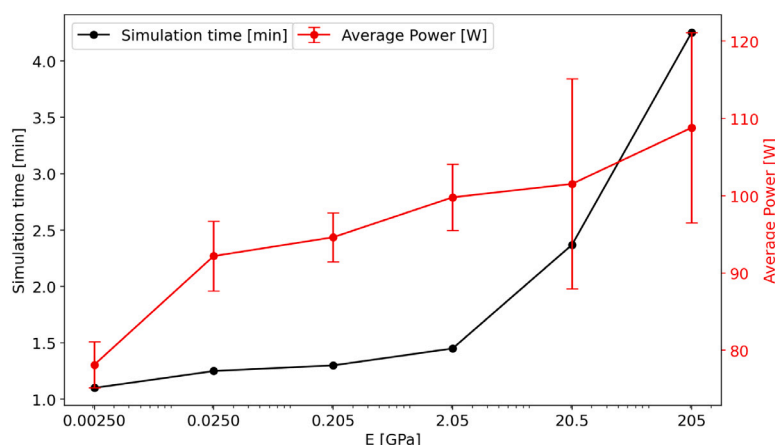
Fig. 4. Young's modulus sensitivity analysis. Red line indicates the simulation's average power and the black line indicates the simulation time. Whiskers show two standard deviations from the corresponding means. Ball size = 10 mm, rotational speed = 1200 rpm.

Table 4
Fill ratio configurations.

Fill ratio (f_r)	Jar volume [ml]	Number of balls ($d_b = 10$ mm)	Number of balls ($d_b = 5$ mm)
0.04		10	76
0.06		14	115
0.08		19	153
0.1		24	191
0.12	125	29	229
0.16		38	306
0.2		48	382
0.3		72	573
0.4		96	764

2.6. Chemicals

Hydrated sodium metaborate ($NaBO_2 \cdot 4\,H_2O$) (≥99%) was obtained from Sigma-Aldrich, while magnesium hydride (MgH_2) (≥99.9%, ≤50 μm) was sourced from Nanoshel. All reagents were used without further purification. The reaction between these reactants facilitates the following conversion:

$$NaBO_2 \cdot 4\,H_2O + 6\,MgH_2 \rightarrow NaBH_4 + 6\,MgO + 8\,H_2 \qquad (27)$$
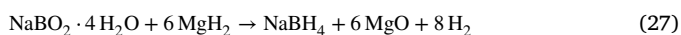
The sample preparation for ball milling was performed in a glove box under an argon atmosphere, with oxygen and water concentrations maintained below 0.1 ppm.

3. Results and discussion

In this section, the performance of the Emax is evaluated in terms of energy and power dissipation in collision events. The motivation for focusing on these parameters is that they represent how kinetic energy is being transformed into usable energy for the mechanochemical reaction to take place [1]. First, the performance is assessed by varying the diameter of the milling balls from 5 mm to 10 mm, and altering the rotational speed from 600 rpm to 1200 rpm while maintaining a consistent fill ratio of 8%. Then, the fill ratio is varied following Table 4, and two rotational speeds are tested. With the obtained results, master curves are built which allow for generalization of the results in terms of the grinding media's density, ball diameter, rotational speed, amplitude (radius) of oscillation, collision frequency, number of balls, and powders used.

3.1. Ball size and rotational speed

We start with an analysis of the performance in energy dissipation as the ball size and rotational speed change while maintaining a constant

fill ratio of 8%. Fig. 5 presents the probability distributions of normal and tangential energy dissipation per cycle for different rotational speeds (600, 800, 1000, and 1200 rpm) and two milling ball diameters: 10 mm and 5 mm. The comparison includes unaltered steel conditions and calibrated conditions, where friction coefficients (static and rolling) and the restitution coefficient have been adjusted.

As expected, higher rotational speeds lead to greater energy dissipation due to the increased kinetic energy available during each cycle, which is reflected in the peak shift from lower values at 600 rpm to higher values at 1200 rpm. A key observation across the plots is that tangential energy dissipation increases at a faster rate, compared to normal dissipation, as the rotational speed increases. This is easier to visualize in Fig. 6 where the mean dissipation values are presented.

The difference between calibrated and non-calibrated values is reflected in a shift of peak dissipation values. In the case of 10 mm balls, this shift is guided towards smaller values whereas in the case of 5 mm balls, the shift is much more subtle and is guided towards larger values. Specifically, this shift causes the mean tangential dissipation to no longer exhibit a significant difference between 5 mm and 10 mm balls, as it did by 13% with the non-calibrated conditions. In contrast, a difference of 20% can now be identified for the mean normal dissipation.

This result indicates that the calibration process is much more critical as the size of the milling balls and the rotational speed increase. Additionally, the standard deviation and coefficient of variation decrease in both directions when smaller milling balls are used, as shown in Table 5. This suggests that the use of smaller milling balls can lead to a more consistent and predictable process, potentially increasing efficiency, if the required energy input for a given mechanochemical reaction is known.

3.2. Fill ratio

The analysis of the fill ratio is crucial as it determines the number of grinding elements involved in the mechanochemical process, impacting both the collision frequency and the milling balls' dynamic behavior. As a consequence, it defines operational ranges that enhance either normal or tangential dissipation. Figs. 7 and 8 show the mean energy dissipation in the normal and tangential directions, as the fill ratio is varied according to Table 4, for unaltered and calibrated conditions, respectively.

For both conditions, it is useful to define three operational zones. The first zone covers a fill ratio from 4% to 10%, the second extends from 10% to 20%, and the third goes from 20% to 40%. In terms of normal dissipation, the optimal operating range falls within the second zone, where the majority of the maximum normal dissipation values are
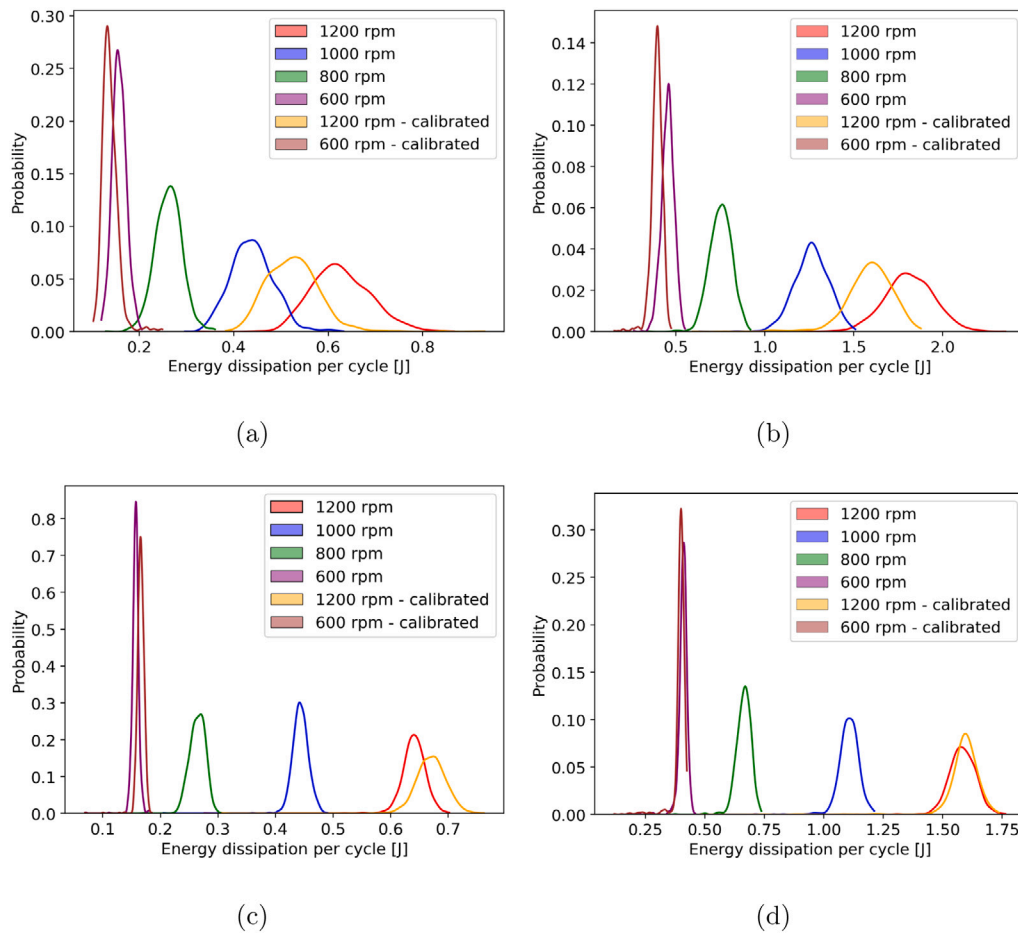
Fig. 5. (a) Normal energy dissipation per cycle, d = 10 [mm] (b) Tangential energy dissipation per cycle, d = 10 [mm] (c) Normal energy dissipation per cycle, d = 5 [mm] (d) Tangential energy dissipation per cycle, d = 5 [mm]. Fill ratio = 8% for all cases.
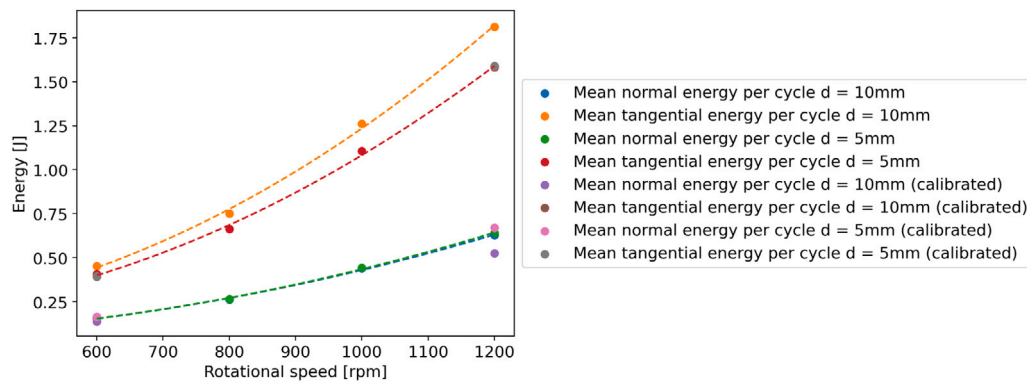

Fig. 6. Mean energy dissipation per cycle. Note that the blue and green curve virtually overlap.

Table 5
Descriptive statistics for energy dissipation per cycle.

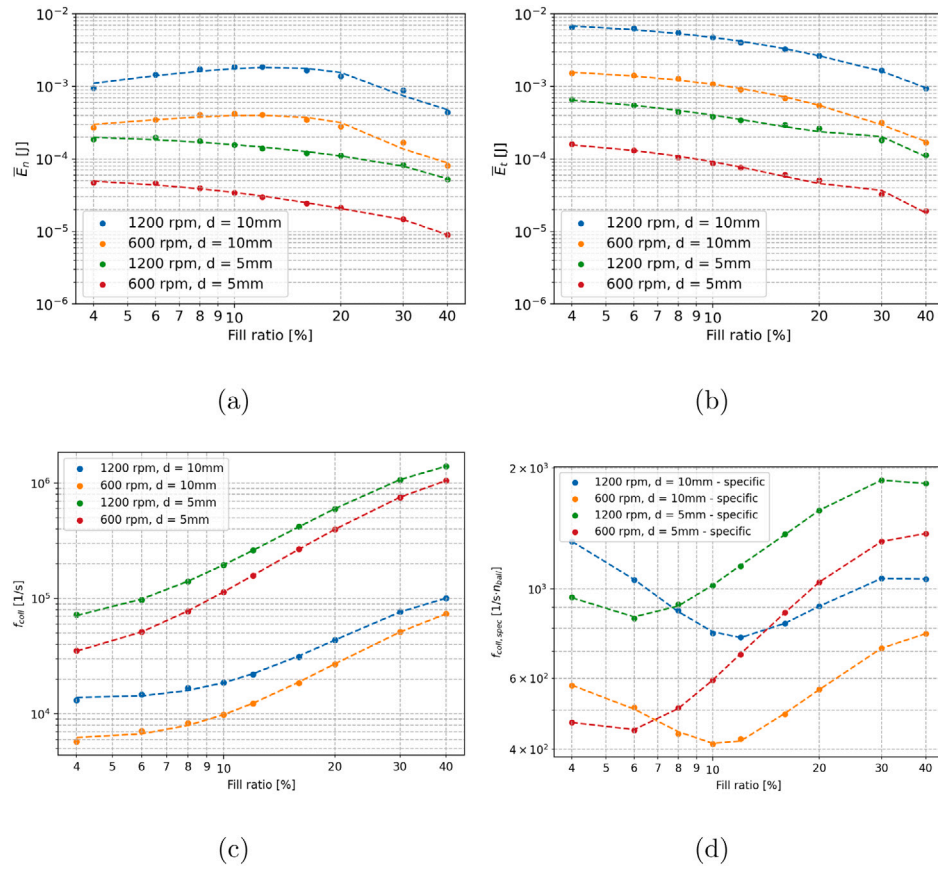|	Normal energy dissipation				Tangential energy dissipation			
	Standard deviation		Coefficient of variation		Standard deviation		Coefficient of variation	
	$d_b = 5$ mm	$d_b = 10$ mm	$d_b = 5$ mm	$d_b = 10$ mm	$d_b = 5$ mm	$d_b = 10$ mm	$d_b = 5$ mm	$d_b = 10$ mm
600 rpm	0.006	0.015	3.81%	9.27%	0.019	0.035	4.70%	7.76%
800 rpm	0.014	0.029	5.45%	10.95%	0.033	0.065	5.03%	8.64%
1000 rpm	0.015	0.046	3.50%	10.36%	0.047	0.098	4.22%	7.77%
1200 rpm	0.023	0.063	3.53%	10.11%	0.064	0.145	4.06%	8.02%

Fig. 7. (a) Mean normal energy per collision $\overline{E}_n$ (b) Mean tangential energy per collision $\overline{E}_t$ (c) Collision frequency f_{coll} (d) Specific collision frequency $f_{coll,spec}$. Cases with fill ratio variation and unaltered steel coefficients.

observed. However, clear differences emerge between unaltered and calibrated coefficients, as well as between small and large milling balls.

Regarding normal dissipation, the most noticeable difference occurs in the transition from zone 1 to zone 2. For large balls, an increase of up to 88% is estimated under calibrated conditions, while unaltered conditions only show an increase of 31%. Interestingly, when using small balls, unaltered conditions display a clear decrease of up to 67%, whereas calibrated conditions remain nearly stable, except at a fill ratio of 4%.

Tangential energy dissipation, on the other hand, exhibits a different behavior. The differences between large and small balls are subtler, with the primary change occurring in how dissipation evolves from zone 1 to zone 2. These results are consistent with the observations in Fig. 6, where a shift from large to small balls led to differences in normal dissipation, but not in tangential dissipation. Under unaltered conditions, tangential dissipation decreases by as much as 150%, making zone 1 optimal for this type of dissipation. Conversely, calibrated conditions show a 42% increase, suggesting that zone 2 remains optimal for tangential dissipation as well.

Finally, when considering collision frequency, both unaltered and calibrated conditions exhibit growth as the number of balls increases, which is expected. However, the rate of growth is notably slower under calibrated conditions. This discrepancy can be explained by the differing behavior of the specific collision frequency in the two scenarios. Under calibrated conditions, the specific collision frequency decreases as the fill ratio increases. This is due to the increased damping, which enhances energy dissipation and reduces the relative velocities between balls. Consequently, collisions per ball occur less frequently as the system becomes denser. In contrast, under unaltered conditions, the lack of realistic damping allows for larger relative velocities, which increase the probability of collisions per ball as the jar becomes more crowded. This upward trend in specific collision frequency amplifies the total collision frequency, resulting in a higher growth rate for unaltered conditions.

Regarding zone 3, it becomes evident that it does not provide any advantages over zones 1 or 2 in terms of energy dissipation. Moreover, the specific collision frequency plateaus in both unaltered and calibrated conditions, indicating the presence of choking behavior. Thus, zone 3 and beyond can be disregarded as zones of interest.

The previously discussed results can be visualized by comparing the heat maps and granular temperatures in Figs. 9 and 10. These maps depict the relative likelihood of finding particles in specific locations in the jar throughout the simulation, offering insight into how the system's dynamics evolve as different fill ratios give rise to the distinct operational zones. With a 4% fill ratio and calibrated coefficients, the combination of fewer balls and increased damping causes the balls to traverse the jar walls with minimal collisions among them, especially when compared to the uncalibrated scenario. This visually explains the significant increase in normal energy dissipation as more balls are added. Furthermore, it clarifies why the tangential dissipation remains almost constant for the calibrated values: most of the tangential dissipation arises from balls scraping along the jar walls. Since the balls maintain contact with the wall throughout the process, tangential dissipation reaches near-maximum values even at low fill ratios.

When examining the maps for the 10% fill ratio, the key difference is that with calibrated coefficients, collisions still do not occur in the center of the jar, unlike in the uncalibrated case. This visual representation also explains why the maximum normal dissipation for calibrated coefficients is achieved by further increasing the fill ratio to around 18%, as opposed to the 10% observed with uncalibrated coefficients. Since most of the normal dissipation results from head-on collisions between balls, allowing them to move slightly further towards the center of the jar leads to maximum dissipation.
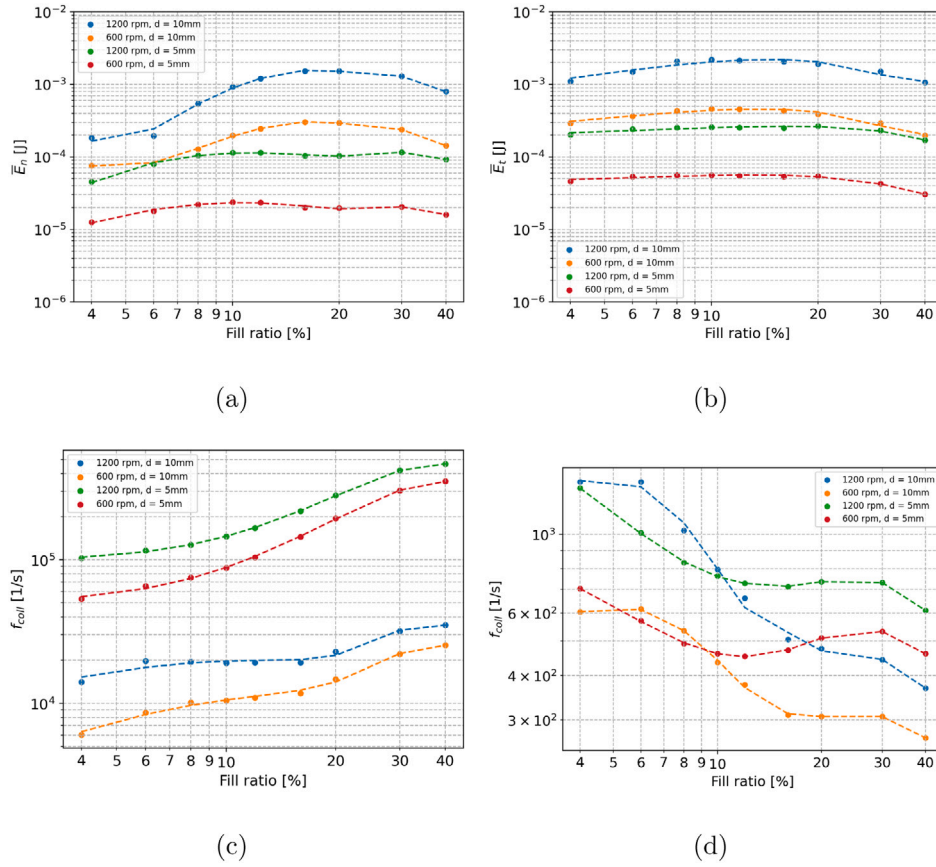
Fig. 8. (a) Mean normal energy per collision $\overline{E}_n$ (b) Mean tangential energy per collision $\overline{E}_t$ (c) Collision frequency f_{coll} (d) Specific collision frequency $f_{coll,spec}$. Cases with fill ratio variation and calibrated coefficients (system comprising $NaBO_2 \cdot 4\,H_2O$ and MgH_2).

Lastly, the map for the 40% fill ratio shows, in both scenarios, why zone 3 is unfavorable. In both cases, there is a clogging effect, where the balls are unable to achieve high-energy collisions anywhere in the jar.

3.3. Master curves

The prior analysis provides a clear description of how the dynamics of the milling balls change as powder is introduced into the milling jar for a mechanochemical reaction. However, two limitations remain. First, while the dissipated energy in each collision is crucial for driving the reaction, it is also important to consider the dissipated power, which accounts for the rate of collisions that generate this energy. Ideally, maximizing power dissipation would combine a high frequency of collisions with the maximum amount of energy dissipated.

The second limitation relates to the fact that these results are, so far, specific to the operating conditions used in the simulations for this work. To address both issues simultaneously, we introduce master curves. These curves are designed to facilitate prediction capabilities when variables such as fill ratio, collision frequency, number of balls, ball density, rotational speed, ball diameter, and amplitude of rotation are varied. This approach offers significant flexibility for both characterization and iterative analysis.

The master curves are constructed using the normalization formulas presented in Eqs. (28) and (29) which are based on basic mechanical principles. As shown in Figs. 11 and 12, these curves provide the mean specific power dissipation, along with the respective standard deviation, for both normal and tangential components. From there, mean energy dissipation values can be obtained by using the corresponding mean specific collision frequency curve.

$$\tilde{P}_{spec} = \frac{f_{col}\bar{E}}{\rho\omega^3 A^2 d_p^3 n_{ball}} \tag{28}$$

$$\tilde{f}_{coll} = \frac{f_{col}}{\omega n_{ball}} \tag{29}$$

where f_{col} is the collision frequency, $\bar{E}$ is mean energy dissipation, ρ is the density of the grinding media, ω is the rotational speed of the mill (in Hz), A is the amplitude of oscillation, d_p is the diameter of the milling balls and n_{ball} is the number of milling balls in the system.

Additionally, Figs. 11(d) and 12(d) show the ratio between the mean specific tangential and normal dissipation powers for the unaltered and calibrated scenarios, respectively. In this plot, it becomes easier to distinguish the three operational zones previously discussed. The first zone goes from 4% to 10% and favors tangential dissipation. At this point, the elbow of the curve can be identified, meaning that this fill ratio provides the best balance between normal and tangential dissipation in this machine. Then, the second zone, which extends up to 20%, increases the relevance of normal dissipation. Lastly, the third zone, extending beyond 20%, provides no benefit as the ratio is no longer able to achieve values beyond those achievable at lower fill ratios. Furthermore, the ratio remains constant in this range since both types of dissipation begin to decay at the same rate. The identification of this limit is convenient as it establishes a clear upper boundary for the number of balls that should be used in the ball mill. Exceeding this value will result in inefficiency.

It is worth highlighting some key differences that arise in the calibrated master curves (see Fig. 12), given that these represent the real system relevant for the mechanochemical regeneration of $NaBH_4$. Specifically, it can be observed that while the maximum zone for normal dissipation remains in the 10%–20% range, the actual fill ratio leading to maximum normal dissipation may fluctuate between 10% and 18% due to the standard deviation of the data. This is explained by the behavior identified in Section 3.1, where it was noted that
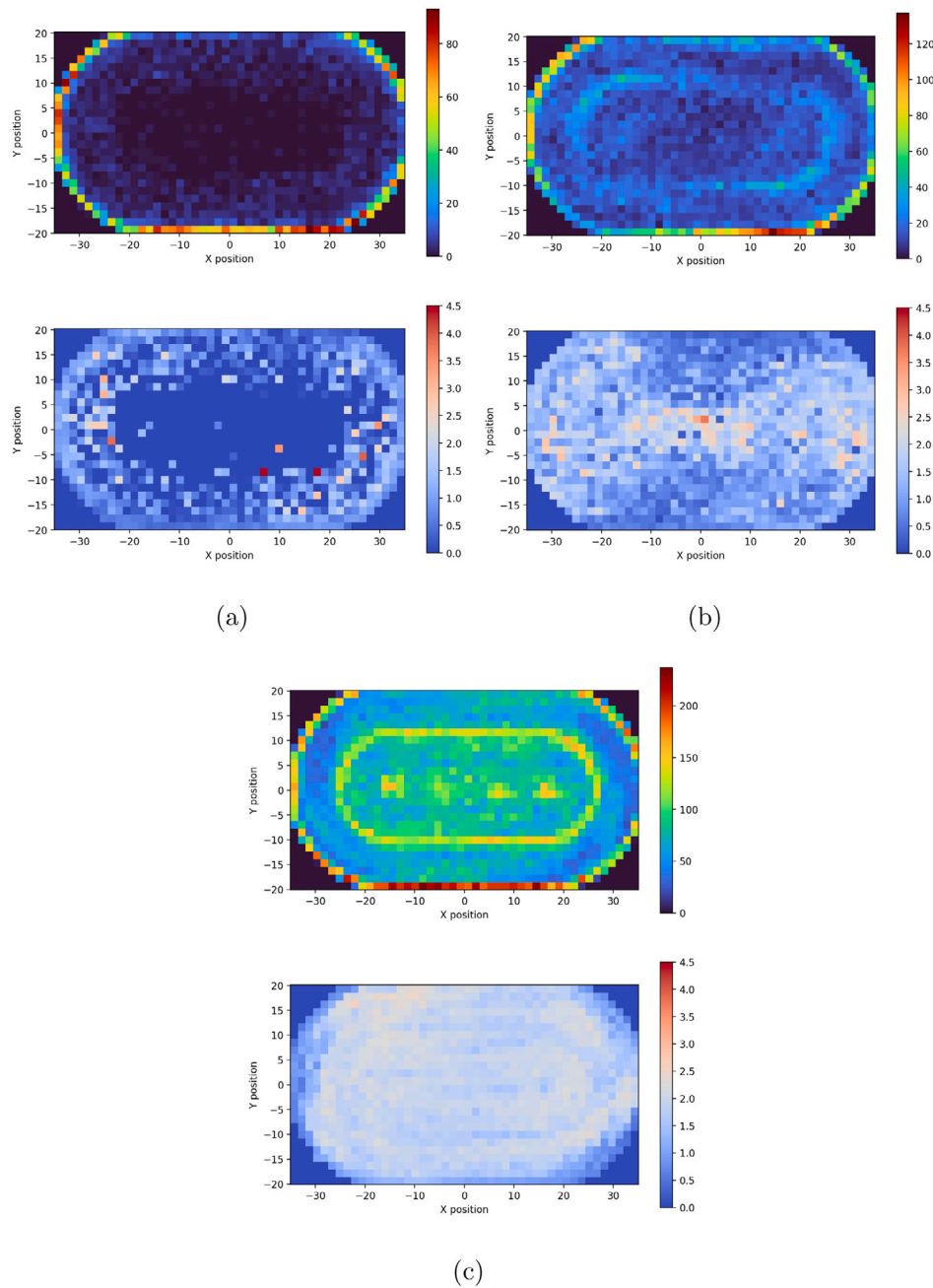
Fig. 9. Particle heat map (blue–green-red) and granular temperature (blue–white-red). $n = 1200$ [rpm] and $d = 10$ [mm]. Fill ratio: (a) 4% (b) 10% (c) 40%. Unaltered steel values.

switching from small balls to large balls shifts the mean normal energy dissipation.

Similarly, while the maximum zone for tangential dissipation remains in the 4%–8% range, the standard deviation in the master curve allows for two interpretations: either a maximum is achieved at 4% or 8%. This variation arises due to the dynamic behavior depicted in Fig. 10(a), as previously discussed. At low fill ratios, the use of 10 mm balls causes energy dissipation to be dominated by collisions with the wall, effectively minimizing the contribution of ball–ball interactions. Smaller balls, however, do not exhibit this condition. Nevertheless, it is expected that if even lower fill ratios are used, collisions between smaller balls will also eventually be minimized, as they will begin to traverse smoothly against the wall of the jar. In this operational range, tangential dissipation can be up to 4 times higher than normal dissipation. The elbow of the curve at 10% results in a ratio of 2.1,

and with higher fill ratios, the ratio between tangential and normal dissipation can be minimized to 1.5.

To conclude, it is worth reiterating that these master curves encompass vastly different operational conditions. While the standard deviation may cause a slightly incorrect selection of the maxima, the master curves remain highly effective for facilitating a mechanical characterization of the regeneration of $NaBH_4$ without the need for additional simulations.

3.4. Testing the master curves

To test the master curves and their capability for characterization and prediction, it is essential to use an existing mechanochemical experiment along with its chemical yield. For this purpose, we utilize
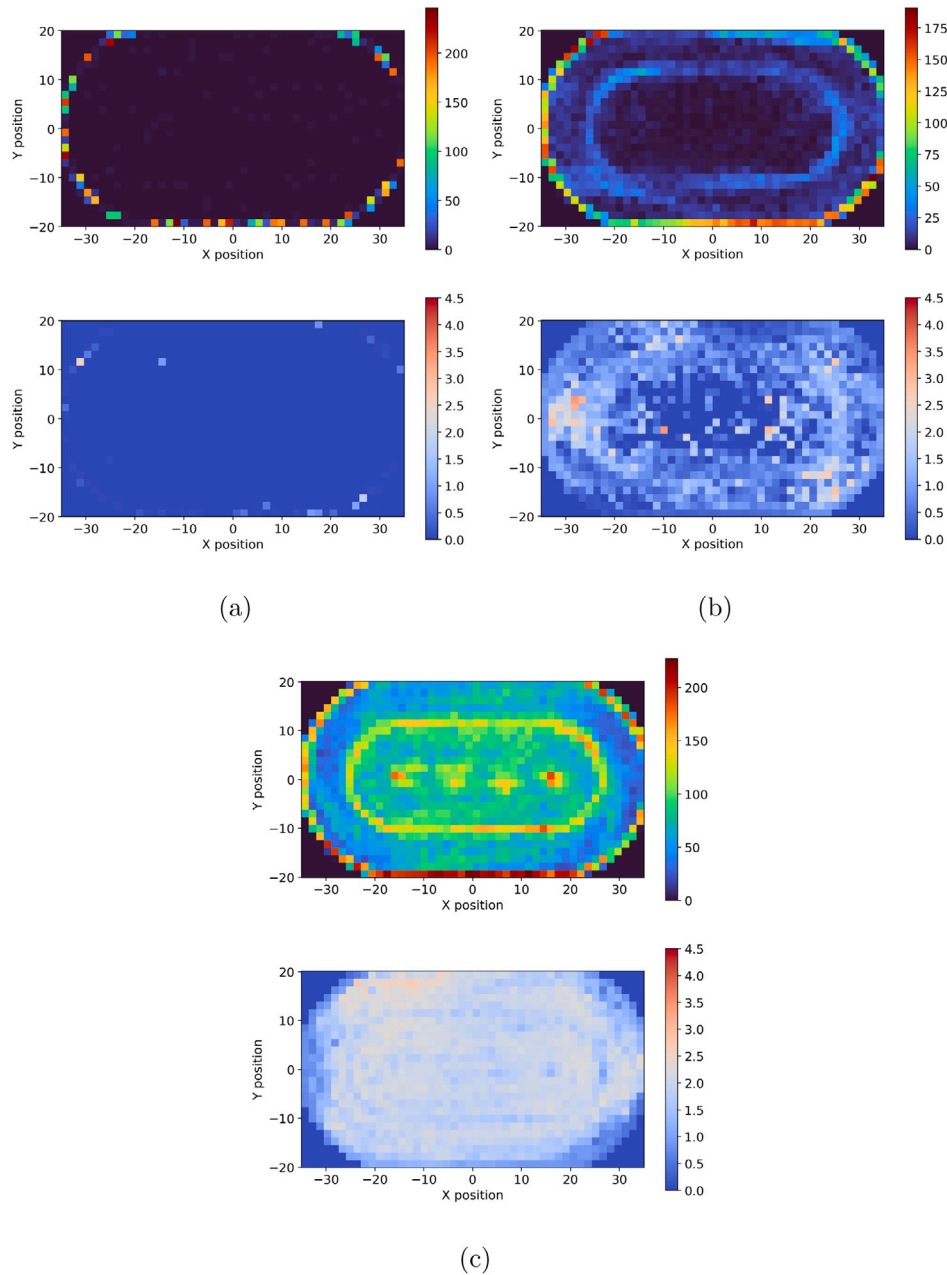
(a)

(b)

(c)

Fig. 10. Particle heat map (blue–green–red) and granular temperature (blue-white-red). n = 1200 [rpm] and d = 10 [mm]. Fill ratio: (a) 4% (b) 10% (c) 40%. Calibrated values.

the same reference case used for calibration. This case involves a ball-to-powder ratio of 30, an excess molar ratio of 66%, a milling time of 12.5 h, a rotational speed of 600 rpm (10 Hz), a fill ratio of 10%, and a ball size of 10 mm. Under these conditions, a $NaBH_4$ regeneration yield of 71% was achieved [19]. By applying our master curves and Eqs. (31) and (32), we can propose a mechanical characterization of the mechanochemical process by defining three main characteristic values: the mean normal energy dissipation $\bar{E}_n$, calculated as 2.21×10^{-4} J; the mean tangential energy dissipation $\bar{E}_t$, calculated as 5.00×10^{-4} J; and a specific collision frequency $\frac{f_{col}}{n_{ball}}$ of 400 s^{-1}.

With these values defined, it is now possible to use the master curves to derive a new set of conditions that can replicate the characteristic mechanical values. We choose to preserve a fill ratio of 10%, as we wish to maintain the ratio between tangential and normal dissipation for this study. However, we opt to use 5 mm balls requiring a total of 191

milling balls; representing a 700% increase over the reference case. By changing the ball size and keeping the three characteristic mechanical values constant, Eq. (31) and Eq. (32) allow us to solve for the density of the balls, rotational speed, or amplitude of rotation. We choose to solve for the rotational speed given the grinding media and equipment available. The new rotational speed is 1698 rpm (28.3 Hz), which represents a 183% increase over the reference case. A new experiment is conducted under these conditions, yielding a regeneration of 67%, just 4% below the reference case of 71%. This experiment was carried out twice to ensure reproducibility (see Fig. 13).

3.5. Universal master curves

In Section 3.3, we presented two distinct sets of master curves, each independently characterizing the mechanical performance of the ball
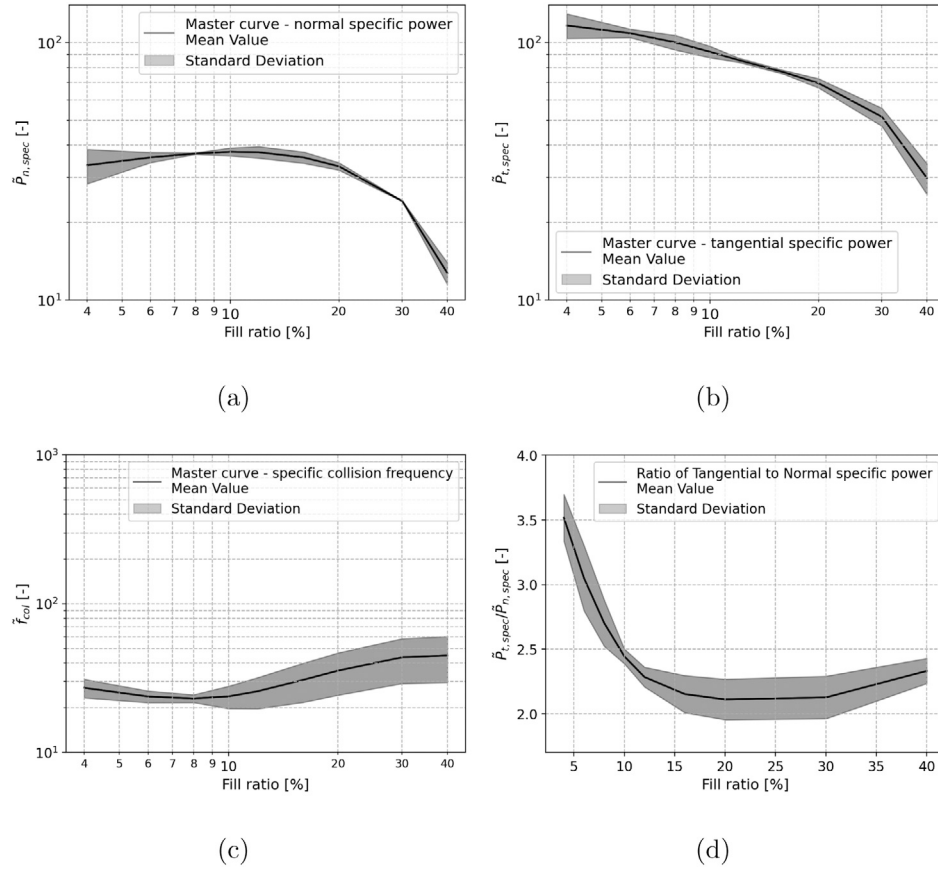
Fig. 11. (a) Master curve - mean specific normal power dissipation per collision $\tilde{P}_{spec,n}$ (b) Master curve - mean specific tangential power dissipation per collision $\tilde{P}_{spec,t}$ (c) Master curve - mean specific collision frequency $\tilde{f}_{coll}$ (d) Ratio between mean specific tangential power dissipation per collision and mean specific normal power dissipation per collision $\frac{\tilde{P}_{spec,t}}{\tilde{P}_{spec,n}}$. Unaltered steel coefficients.

mill under different friction coefficients, which vary according to the presence of processed material. To develop a universal master curve that can characterize any processed material with calibrated coefficients within the ranges addressed in this work (restitution coefficient: 0.3–0.7, static friction coefficient: 0.3–0.69), we utilize the effective restitution coefficient, ε, as defined by Chialvo and Sundaresan [26].

$$\varepsilon = e - \frac{3}{2}\mu \exp(-3\mu) \tag{30}$$

where e is the standard restitution coefficient, and μ is the static friction coefficient (see Fig. 14).

Thus, general equations for constructing universal master curves can be proposed as follows:

$$\tilde{P}_{spec} = \frac{f_{col}\bar{E}}{\rho\omega^3 A^2 d_p^3 n_{ball}} \cdot (1-\varepsilon)^{1/2} \tag{31}$$

$$\tilde{f}_{coll} = \frac{f_{col}}{\omega n_{ball}} \cdot (1-\varepsilon)^{1/2} \tag{32}$$

To use these curves effectively, it is necessary to first obtain calibrated values for the restitution coefficient and static friction coefficient to calculate ε. These universal curves are less accurate than the specific-case curves (Figs. 11 and 12) because they do not apply exclusively to a specific set of contact parameters. They aim to capture the dynamic changes caused by adding different processed materials to the milling jar and their impact on the motion of the milling balls. Despite this decrease in accuracy, the universal curves remain a practical and efficient tool for estimating dissipation mechanisms without requiring additional simulations. Moreover, while the utility of this characterization methodology has been tested for the system

comprising $NaBO_2 \cdot 4\,H_2O$ and MgH_2, it still needs to be tested for other mechanochemical processes.

4. Conclusions

In this paper, we have presented a comprehensive study of the mechanical interactions that govern high-energy ball milling for mechanochemistry purposes by focusing on a distinction between normal and tangential energy dissipation. Our findings present a clear methodology that can be followed to obtain an in-depth characterization of any milling machine. By following it, the development of green chemical processes can be facilitated and their generalization and reproducibility across scales and setups becomes viable.

We used the Hertz–Mindlin model and discrete element modeling to accurately characterize the forces involved in ball–ball and ball–wall collisions, allowing us to distinguish the contribution of normal and tangential interactions in the mechanical energy dissipation of the system. Our approach allowed us to identify optimal operational ranges where each form of dissipation can thrive and to characterize the milling process with master curves that predict the performance of the mill under different conditions beyond those presented in this work.

We also found that the contribution of tangential interactions to the mechanical energy dissipation of the system is significant and cannot be neglected as it dominates the overall dissipation. This is particularly important for use cases where shearing has the potential to be a critical component leading to a successful outcome. Moreover, maximizing or minimizing its significance in the global energy dissipation performance is possible by varying the fill ratio.
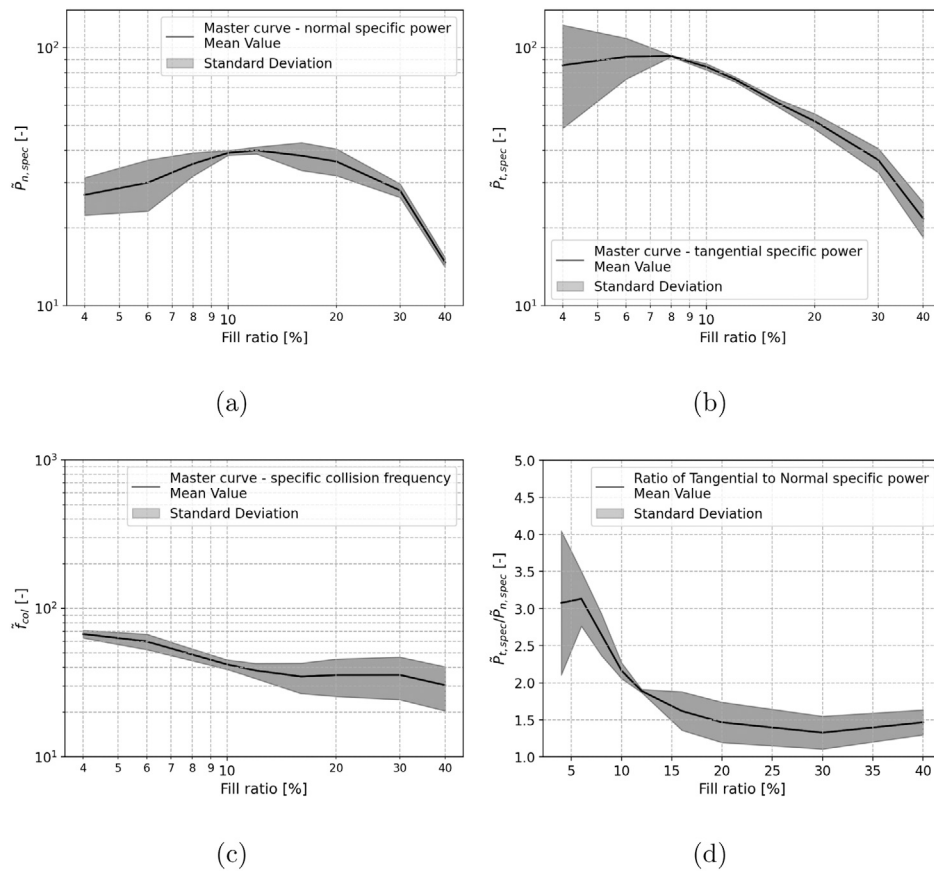
Fig. 12. (a) Master curve - mean specific normal power dissipation per collision $\tilde{P}_{spec,n}$ (b) Master curve - mean specific tangential power dissipation per collision $\tilde{P}_{spec,t}$ (c) Master curve - mean specific collision frequency $\tilde{f}_{coll,spec}$ (d) Ratio between mean specific tangential power dissipation per collision and mean specific normal power dissipation per collision $\frac{\tilde{P}_{spec,t}}{\tilde{P}_{spec,n}}$. Calibrated coefficients (system comprising $NaBO_2 \cdot 4H_2O$ and MgH_2).
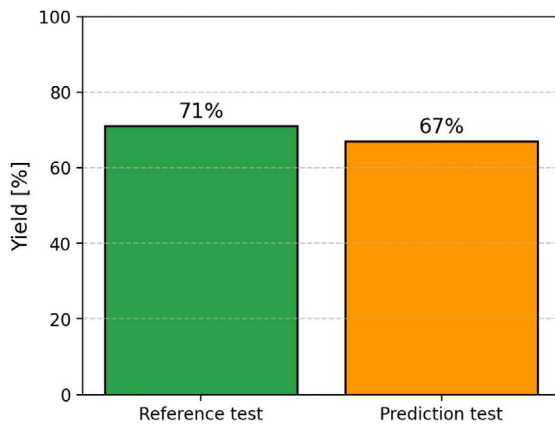

Fig. 13. Mechanochemical yield in reference case and predicted case.

The performance of the milling machine is strongly influenced by the milling parameters, such as the ball size, fill ratio, and rotational speed. Our master curves present a valuable tool for designing, optimizing, and predicting mechanochemical processes. Additionally, they enable a direct comparison of key mechanical conditions among different milling machines thanks to the dimensional analysis carried out.

This work presents the first mechanical characterization for the mechanochemical regeneration of $NaBH_4$. By establishing the mean normal energy dissipation, mean tangential energy dissipation, and specific collision frequency as process parameters, we successfully predicted a new set of conditions that replicated a previously achieved result with only a 4% difference.

This work represents a step forward in the understanding of the complex behavior of mechanical forces in high-energy ball milling and their influence on the success of mechanochemical reactions. Future work will focus on studying how different ratios between tangential and normal dissipation affect the success of the regeneration of $NaBH_4$. We hope that our findings will inspire further research in this field and contribute to the development of more efficient and sustainable chemical processes.

CRediT authorship contribution statement

Santiago Garrido Nuñez: Writing – review & editing, Writing – original draft, Visualization, Validation, Methodology, Investigation, Formal analysis, Data curation, Conceptualization. **Dingena L. Schott:** Writing – review & editing, Supervision, Formal analysis. **Johan T. Padding:** Writing – review & editing, Funding acquisition, Formal analysis, Conceptualization.
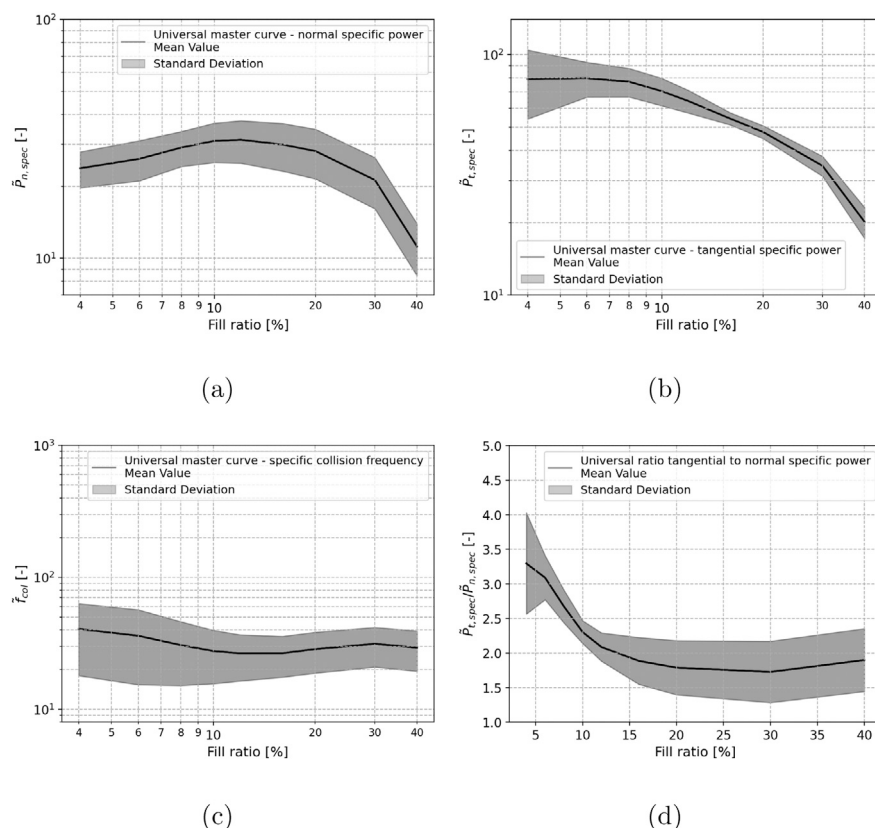
Funding

Fig. 14. (a) Universal master curve - mean specific normal power dissipation per collision $\tilde{P}_{spec,n}$ (b) Universal master curve - mean specific tangential power dissipation per collision $\tilde{P}_{spec,t}$ (c) Universal master curve - mean specific collision frequency $\tilde{f}_{coll,spec}$ (d) Universal ratio between mean specific tangential power dissipation per collision and mean specific normal power dissipation per collision $\frac{\tilde{P}_{spec,t}}{\tilde{P}_{spec,n}}$.

Declaration of competing interest

The authors declare the following financial interests/personal relationships which may be considered as potential competing interests: Johan T. Padding reports financial support was provided by Netherlands Enterprise Agency. If there are other authors, they declare that they have no known competing financial interests or personal relationships that could have appeared to influence the work reported in this paper.

Data availability

Data will be made available on request.

References

[1] Valentina Martinez, Tomislav Stolar, Bahar Karadeniz, Ivana Brekalo, Krunoslav Užarević, Advancing mechanochemical synthesis by combining milling with different energy sources, Nat. Rev. Chem. 7 (1) (2023) 51–65, http://dx.doi.org/10.1038/s41570-022-00442-1.

[2] Jean-Louis Do, Tomislav Friščić, Mechanochemistry: A force of synthesis, ACS Cent. Sci. 3 (1) (2017) 13–19, http://dx.doi.org/10.1021/acscentsci.6b00277, arXiv:https://doi.org/10.1021/acscentsci.6b00277. PMID: 28149948.

[3] Helder Nunes, Diogo Silva, Carmen Rangel, Alexandra Pinto, Rehydrogenation of sodium borates to close the NaBH$_4$-H$_2$ cycle: A review, Energies 14 (2021) 3567, http://dx.doi.org/10.3390/en14123567.

[4] Luz María Martínez, Jorge Cruz-Angeles, Mónica Vázquez-Dávila, Eduardo Martínez, Paulina Cabada, Columba Navarrete-Bernal, Flor Cortez, Mechanical activation by ball milling as a strategy to prepare highly soluble pharmaceutical formulations in the form of co-amorphous, co-crystals, or polymorphs, Pharmaceutics 14 (10) (2022) http://dx.doi.org/10.3390/pharmaceutics14102003, URL https://www.mdpi.com/1999-4923/14/10/2003.

[5] Victor A. Rodriguez, Luciane Ribas, Arno Kwade, Luís Marcelo Tavares, Mechanistic modeling and simulation of a wet planetary ball mill, Powder Technol. 429 (2023) 118901, http://dx.doi.org/10.1016/j.powtec.2023.118901, URL https://www.sciencedirect.com/science/article/pii/S003259102300685X.

[6] Francesco Delogu, Laszlo Takacs, Information on the mechanism of mechanochemical reaction from detailed studies of the reaction kinetics, J. Mater. Sci. 53 (19) (2018) 13331–13342, http://dx.doi.org/10.1007/s10853-018-2090-1.

[7] Wenliang Chen, Mirko Schoenitz, Trent Ward, Rajesh Dave, Edward Dreizin, Numerical simulation of mechanical alloying in a shaker mill by discrete element method, KONA Powder Part. J. 23 (2005) 152–162, http://dx.doi.org/10.14356/kona.2005018.

[8] M. Broseghini, M. D'Incau, L. Gelisio, N.M. Pugno, P. Scardi, Effect of jar shape on high-energy planetary ball milling efficiency: Simulations and experiments, Mater. Des. 110 (2016) 365–374, http://dx.doi.org/10.1016/j.matdes.2016.06.118, URL https://www.sciencedirect.com/science/article/pii/S0264127516308802.

[9] Christine Burmeister, Robert Schmidt, Katharina Jacob, Sandra Breitung, Achim Stolle, Arno Kwade, Effect of stressing conditions on mechanochemical knoevenagel synthesis, Chem. Eng. J. 396 (2020) 124578, http://dx.doi.org/10.1016/j.cej.2020.124578.

[10] Christine F. Burmeister, Achim Stolle, Robert Schmidt, Katharina Jacob, Sandra Breitung-Faes, Arno Kwade, Experimental and computational investigation of knoevenagel condensation in planetary ball mills, Chem. Eng. Technol. 37 (5) (2014) 857–864, http://dx.doi.org/10.1002/ceat.201300738, arXiv:https://onlinelibrary.wiley.com/doi/pdf/10.1002/ceat.201300738. URL https://onlinelibrary.wiley.com/doi/abs/10.1002/ceat.201300738.

[11] Chan-Li Hsueh, Cheng-Hong Liu, Bing-Hung Chen, Chuh-Yung Chen, Yi-Chia Kuo, Kuo-Jen Hwang, Jie-Ren Ku, Regeneration of spent-NaBH$_4$ back to NaBH$_4$ by using high-energy ball milling, Int. J. Hydrog. Energy 34 (4) (2009) 1717–1725, http://dx.doi.org/10.1016/j.ijhydene.2008.12.036, URL https://www.sciencedirect.com/science/article/pii/S0360319908016662.

[12] A.L.R. Oliveira, V.A. Rodriguez, R.M. de Carvalho, M.S. Powell, L.M. Tavares, Mechanistic modeling and simulation of a batch vertical stirred mill, Miner. Eng. 156 (2020) 106487, http://dx.doi.org/10.1016/j.mineng.2020.106487, URL https://www.sciencedirect.com/science/article/pii/S0892687520303071.

[13] S. Beinert, G. Fragnière, C. Schilde, A. Kwade, Analysis and modelling of bead contacts in wet-operating stirred media and planetary ball mills with

CFD–DEM simulations, Chem. Eng. Sci. 134 (2015) 648–662, http://dx.doi.org/10.1016/j.ces.2015.05.063, URL https://www.sciencedirect.com/science/article/pii/S0009250915004030.

[14] Altair Engineering Inc., The Hertz-Mindlin (no slip) model. URL https://help.altair.com/EDEM/Creator/Physics/Base_Models/Hertz-Mindlin_(no_slip.htm).

[15] DCS Computing GmbH, JKU Linz and Sandia Corporation, Gran model hertz model. URL https://www.cfdem.com/media/DEM/docu/gran_model_hertz.html.

[16] Christine Burmeister, Moritz Hofer, Palanivel Molaiyan, Peter Michalowski, Arno Kwade, Characterization of stressing conditions in a high energy ball mill by discrete element simulations, Processes 10 (2022) 692, http://dx.doi.org/10.3390/pr10040692.

[17] Priya Santhanam, Edward Dreizin, Predicting conditions for scaled-up manufacturing of materials prepared by ball milling, Powder Technol. 221 (2012) 403–411, http://dx.doi.org/10.1016/j.powtec.2012.01.037.

[18] S. Rosenkranz, S. Breitung-Faes, Arno Kwade, Experimental investigations and modeling of the ball motion in planetary ball mills, Powder Technol. 212 (2011) 224–230, http://dx.doi.org/10.1016/j.powtec.2011.05.021.

[19] Santiago Garrido Nuñez, Dingena L. Schott, Johan T. Padding, Optimization of operational parameters in the mechanochemical regeneration of sodium borohydride (NaBH4), Int. J. Hydrog. Energy 97 (2025) 640–648, http://dx.doi.org/10.1016/j.ijhydene.2024.11.360, URL https://www.sciencedirect.com/science/article/pii/S0360319924050511.

[20] Chandana Jayasundara, Haiping Zhu, Impact energy of particles in ball mills based on DEM simulations and data-driven approach, Powder Technol. 395 (2021) http://dx.doi.org/10.1016/j.powtec.2021.09.063.

[21] D.R. Lide, CRC Handbook of Chemistry and Physics, ninetieth ed., Taylor & Francis, 2009, URL https://books.google.nl/books?id=OmkbNgAACAAJ.

[22] Lucefin Group, X46Cr13 technical card. URL https://www.lucefin.com/wp-content/files_mf/1.4034a420c25.pdf.

[23] Isaac Goldhirsch, Introduction to granular temperature, Powder Technol. 182 (2) (2008) 130–136, http://dx.doi.org/10.1016/j.powtec.2007.12.002, URL https://www.sciencedirect.com/science/article/pii/S0032591007006109. Granular Temperature.

[24] Ronald W. Breault, Christopher P. Guenther, Lawrence J. Shadle, Velocity fluctuation interpretation in the near wall region of a dense riser, Powder Technol. 182 (2) (2008) 137–145, http://dx.doi.org/10.1016/j.powtec.2007.08.018, URL https://www.sciencedirect.com/science/article/pii/S0032591007004627. Granular Temperature.

[25] Stef Lommen, Dingena Schott, Gabriel Lodewijks, DEM speedup: Stiffness effects on behavior of bulk material, Particuology 12 (2014) 107–112, http://dx.doi.org/10.1016/j.partic.2013.03.006, URL https://www.sciencedirect.com/science/article/pii/S1674200113001387. Special issue on conveying and handling of particulate solids – Challenges of discrete element simulation, application and calibration.

[26] Sebastian Chialvo, Sankaran Sundaresan, A modified kinetic theory for frictional granular flows in dense and dilute regimes, Phys. Fluids 25 (7) (2013) 070603, http://dx.doi.org/10.1063/1.4812804, arXiv:https://pubs.aip.org/aip/pof/article-pdf/doi/10.1063/1.4812804/15710561/070603_1_online.pdf.